Received: 6 October 2024 | Accepted: 10 July 2025

DOI: 10.1111/aos.17566

Acta Ophthalmologica

ORIGINAL ARTICLE

Reproducibility in the identification of retinal positions on serial fundus photographs: Theory and limitations

Toke Bek[1] | **Giovanni Ometto**[2]

[1]Department of Ophthalmology, Aarhus University Hospital, Aarhus, Denmark

[2]City University of London, London, UK

Correspondence
Toke Bek, Department of Ophthalmology, Aarhus University Hospital, Aarhus N DK-8200, Denmark.
Email: toke.bek@mail.tele.dk

Abstract

Background: Imaging of the retina is accompanied by distortions so that positions in fundus photographs cannot be linearly translated to positions in the retinal fundus. The purpose of this study was to describe an algorithm and evaluate its reproducibility in identifying points on the retina from their representation on serial fundus photographs.

Methods: A mathematical formalism was derived to describe how the location of the fovea and the optic disc in fundus photographs, together with the centre-nodal point distance (d) and the curvature radius (r) of the eye, can be used to calculate spatial coordinates on the retina that correspond to given locations in the photograph. The effect of manual markings of the fovea and the optic disc as reference points was evaluated, and the formalism was tested on 105 photographs recorded with different image modalities and centring from 10 different patients.

Results: Retinal locations could be identified in serial fundus photographs with a reproducibility of at least 50 μm when the centre-nodal point distance and the curvature radius were set to those in Gullstrand's standard eye. A main source of the variability was the manual identification of the fovea and optic disc used as reference points.

Conclusions: The reproducibility in the identification of locations on the retina from serial fundus photographs depends on the accuracy in the definition of the fovea and optic disc used as reference points. This affects the potential for describing locations, distances, areas and changes in retinal lesions on serial photographs over time.

KEYWORDS
fundus photography, image processing, optical distortion, retinopathy grading

1 | INTRODUCTION

A standard examination of the retina includes the study of retinal morphology through the optics of the eye. The examination is often documented by fundus photography, but this imaging modality is accompanied by distortions so that observed distances in the image of the retina do not correspond to true distances in the retinal fundus (Bennett et al., 1994). This may have implications for the interpretation of perceived shapes, locations, distances and areas on the photographic representation of the retina. In addition, variations in the distortion of retinal morphology resulting from differences in centring of serial fundus photographs may have an impact on the conclusions that can be made about the development of retinal disease.

Various projection techniques have been designed to overcome this challenge. These approaches include warping of peripheral areas on the basis of vascular landmarks so that all pixels in the image represent the same area on the retina (Spaide, 2011), projection of the retina on the equatorial plane of the eye to allow calculations of areas on the sphere (Croft et al., 2014; Zhang et al., 2023) and studies of the photographic representation of implanted objects with known size (Aboshiha et al., 2015). These techniques allow a quantification of relative distances and areas of the retina. However, due to the lack of inclusion of the ocular size together

with at least two reference points for the calculation of coordinates, the techniques are not optimal for assessing the true positions and the changes in shape, spatial location and dynamics of morphological lesions in the retina over time.

The purpose of this study was to describe and assess the reproducibility of an algorithm where axial distances in the eye together with the location of the fovea and the optic disc are used to align retinal locations on serial fundus photographs. The limitations and possible applications of the technique will be described.

2 | MATERIALS AND METHODS

2.1 | Algorithm

Figure 1 shows a schematic representation of the eye at the equator seen from above, which will be used as a template in the following. The origin of a coordinate system is positioned in the nodal point (N) of the eye, which is an imaginary point located in the posterior part of the lens in which rays incident from different directions in the visual space pass unrefracted to the retina (Harris, 2010). The angle of incidence of a light ray at the nodal point defines the nodal angle (v) to each point (P) on the retina. In the depicted coordinate system, the z-axis follows the visual axis to the fovea (F), whereas the horizontal x-axis and the y-axis, perpendicular to the drawing, are in the frontal plane and thereby correspond to coordinates in a fundus photograph. The centre (C) of the eye is located a distance d from N along the z-axis, and the distance from this centre to all locations on the retina is assumed to equal a constant curvature radius (r).

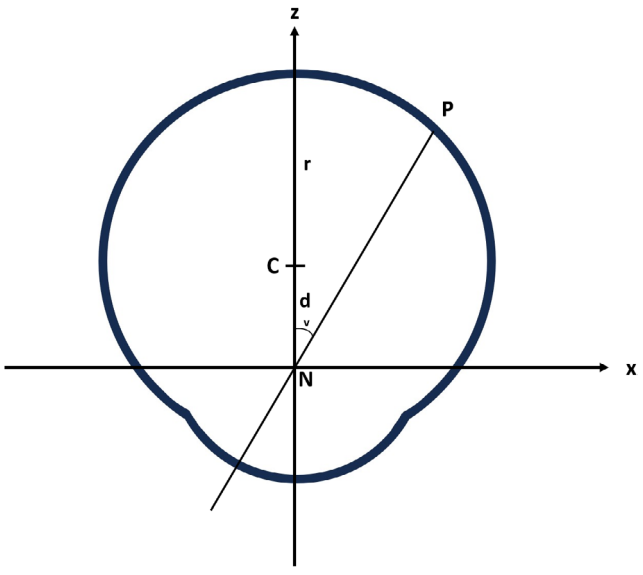

FIGURE 1 The correspondence between an eccentricity in a fundus photograph and a point (P) on the retina. The connecting line passes through the nodal point (N) of the eye at angle (v). N is located distance d in front of the centre of the eye with a curvature radius r.

2.2 | Fovea centred photograph

2.2.1 | Position on fundus photograph

Each position on a fundus photograph corresponds to a position on the retina, and if the camera has a telecentric ray path, equiangular distances in the fundus are imaged equidistantly on the fundus photograph (Littmann, 1982). This implies that for a photograph centred on the fovea, the nodal angle (v) between the fovea and a given point P on the retina can be expressed by the linear distance (l) from the representations of the fovea and the point in the fundus photograph, divided by the total linear width (L) of the photograph and multiplied by its total angular subtense (w) as follows:

$$v = w * \frac{l}{L} \tag{1}$$

2.2.2 | Translation of nodal angle to centre angle

Figure 2 shows how the nodal angle (v_P) to a point P can be translated to the centre angle (ω_P) of the point in a fovea centred photograph in the horizontal plane. It appears that:

$$a = r * \sin(\omega_P) \tag{2}$$

$$b = r * \cos(\omega_P) \tag{3}$$

$$\tan(v_P) = \frac{a}{b+d} \tag{4}$$

The insertion of (2) and (3) in (4) with a following isolation of ω_P is shown in detail in Appendix A. The resulting formula is as follows:

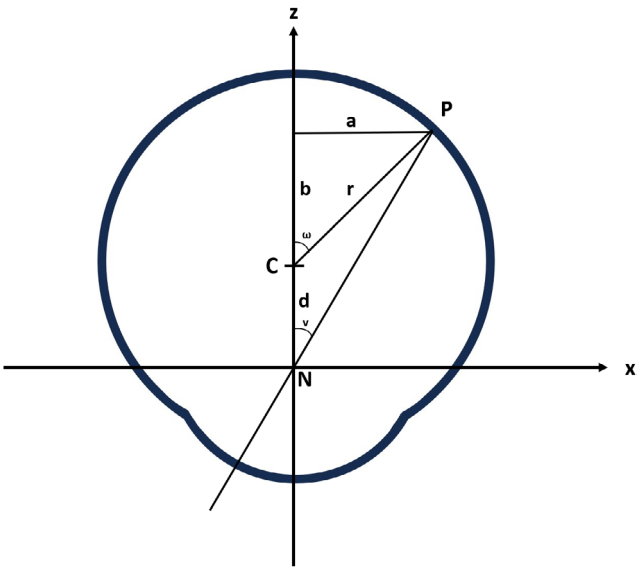

FIGURE 2 The transformation of the nodal angle (v) to the centre angle (ω). Distance a is the opposite and distance b is the adjacent side to angle (ω) in the triangle where (r) constitutes the hypotenuse.

$$\omega_P = a\cos\left(\frac{-d*\tan(v_P)+\sqrt{r^2*\left(1+\frac{1}{\tan^2(v_P)}\right)-d^2}}{r*\left(\tan(v_P)+\frac{1}{\tan(v_P)}\right)}\right) \quad (5)$$

The special case where $v=0$ implies that $\omega_P=0$.

2.2.3 | Calculation of *x*,*y*-coordinates

From Figure 2, it appears that when P is located in the horizontal plane, the *x*-coordinate equals distance a, which can be calculated in the length unit of *r* as:

$$x = a = r*\sin(\omega_P) \quad (6)$$

However, point P may not be in the horizontal plane but may be rotated around the *z*-axis. This implies that the translation from nodal angle to centre angle in Equation (5) should be performed both along the *x*-axis to find (ω_{Px}) and along the *y*-axis to find (ω_{Py}). Subsequently, the *x*,*y* coordinates to point P in the length unit of *r* can be derived as follows:

$$x = a_x = r*\sin(\omega_{Px}) \quad (7)$$

$$y = a_y = r*\sin(\omega_{Py}) \quad (8)$$

2.2.4 | Calculation of *z*-coordinate

The *z*-coordinate will be independent of the rotation around the *z*-axis. Accordingly, the centre angle to the point in the *x*,*y*-plane can be calculated as:

$$\omega_{Pxy} = \sqrt{(\omega_{Px})^2+(\omega_{Py})^2} \quad (9)$$

From Figure 2, it subsequently appears that the *z*-coordinate to point (P) in the length unit of *r* and *d* can be calculated as follows:

$$z = d + b = d + r*\cos(\omega_{Pxy}) \quad (10)$$

2.3 | Photograph with extrafoveal centring

If the photograph has been centred on an extrafoveal point, the calculation of coordinates from Equations (7)–(10) should be preceded by a correction for this decentring. The disadvantage of the movement out of centre is that the photographic plane will become oriented obliquely to the fundus and consequently that parts of the image will become blurred because it is out of focus. However, this does not affect the angles projecting to the points out of focus. The correction for the decentring consists of a rotation of the photograph so that the fovea is in the horizontal plane, followed by a horizontal movement of the fovea to the centre of the photograph.

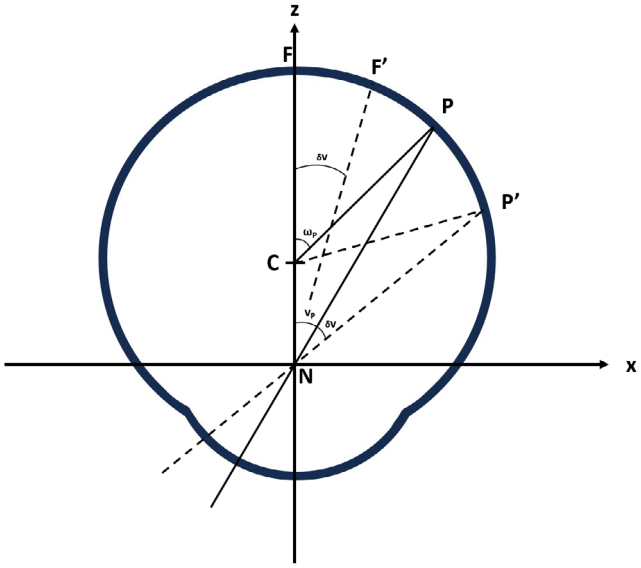

FIGURE 3 The decentring of the photograph by the movement of the fovea with angle d*v* from F to F′ results in a change in the nodal angle by d*v* for all points P to P′ along the direction of the decentring.

2.3.1 | Rotation

The rotation of positions on the photograph around the image centre until the fovea is in the horizontal plane will change the *x*- and *y*-coordinates of retinal points represented in the photograph, whereas the *z*-coordinate of these points will remain unchanged.

2.3.2 | Horizontal movement

The horizontal movement to correct the decentring that remains after the rotation will change distances in the direction of the movement, but not perpendicularly to the movement. Therefore, the correction for decentring will affect distances in the *x*,*z* plane but not along the *y*-axis.

Figure 3 shows that in the rotated position, the magnitude of the movement corresponds to a nodal angle displacement δ*v* of the fovea (*F*) from the image centre to position (*F*′) which can be determined from Equation (1).

The horizontal movement of the fovea with angle δ*v* and the coupled movement of extrafoveal point P with the same angle δ*v* to P′, will lead to a corresponding change in the centre angle in the horizontal plane $\omega_{Px'}$ that can be derived according to the principles in Equation (5) as:

$$\omega_{Px'} = a\cos\left(\frac{-d*\tan(v+\delta v)+\sqrt{r^2*\left(1+\frac{1}{\tan^2(v+\delta v)}\right)-d^2}}{r*\left(\tan(v+\delta v)+\frac{1}{\tan(v+\delta v)}\right)}\right) \quad (11)$$

This corrected value for the centre angle of the point in the horizontal plane should subsequently be inserted instead of ω_{Px} in Equations (7), (9) and (10) above for the calculation of the *x* and *z* coordinates of the point.

2.4 | Correction for image rotation

After the correction for decentring and the calculation of x,y,z-coordinates from positions in the photograph, there is a need for a correction for rotation around the z-axis resulting from cyclotorsion of the eye during photography and rotations of coordinates performed in order to adjust for decentring. This requires the definition of a reference meridian such as the line connecting the fovea and the centre of the optic disc in the x,y-plane. The fovea is already in the centre of the image, and the correction can therefore be performed by rotating the image until the ordinate value of the centre of the optic disc is equal to zero.

2.5 | Testing of camera optics

The Topcon S-5.37D, RM-A6000 model eye (Topcon Europe Medical BV, Essenbaan, Netherlands) was used to test imaging through the following fundus cameras that had been used for recording the fundus photographs used in the study: Canon UV-60 with images recorded on diapositives and scanned to digital format, Canon CF-1 with EOS400 backend, Topcon TRC50DX and the NIDEK RS-300. The model eye was dimensioned according to Gullstrand's standard eye (Gullstrand, 1909) and had markings with 1-degree intervals until 25 degrees on each side of the centre (Topcon Europe Medical B.V, Technical Reference 20061013.1). Imaging through all the tested cameras showed that equiangular distances at the retinal plane were imaged equidistantly on the fundus photograph, which ensured that the light path was telecentric (Littmann, 1982).

2.6 | Fundus photographs

At request, the regional ethics committee informed that the anonymized use of already sampled fundus photographs does not require ethical approval. Therefore, fundus photographs were obtained from the retina clinic at the Department of Ophthalmology, Aarhus University Hospital. The intended centring of the photographs had been on the fovea or elsewhere, often at the optic disc (Aldington et al., 1995). Seven different digital formats (F1-7) had been used to generate photographs with the following horizontal angular widths in degrees and digital resolutions in pixels: F1: 45, [3000 × 2672], F2: 45, [3030 × 2033], F3: 60, [3040 × 2016], F4: 50, [3888 × 2592], F5: 50, [4256 × 2848], F6: 50, [4928 × 3264] and F7: 50, [4988 × 2848]. For each image type, the number of pixels per degree was calculated by disregarding the peripheral rim of the image not covering the photographic field of view.

2.7 | Marking software

The validation of the algorithm required an identification of coordinates in fundus photographs to be transformed to space coordinates. This was performed using the software GRADING PROGRAM (vs. 1.1.1.2, Ocuco, Dublin, Ireland) that allows the marking of (x,y) coordinates for individual points or areas in a fundus photograph. The fovea was marked with a cross and the optic disc by following its edge with the computer mouse along its circumference, which the software subsequently adjusted to the best fitting ellipse. Different types of lesions could be marked, either as single coordinates or as areas containing sets of coordinates, each visualized by a specific colour code. Subsequently, the markings were stored in a text file.

2.8 | Reproducibility in the definition of reference coordinates

In each of 10 randomly selected persons with no sign of retinal disease, the first fovea-centred fundus photographs that were considered to have a clearly identifiable fovea and optic disc were identified. The random sample was represented by five of the seven available image formats(number): F1(1), F3(2), F4(2), F5(2) and F7(3). Each of the 10 images was subsequently copied and inverted horizontally, vertically and both horizontally and vertically to result in altogether 40 photographs that were numbered in random order. Four experienced graders of diabetic retinopathy loaded each photograph in the Fundus Grading programme, marked the fovea and outlined the optic disc and noted the (x,y) pixel coordinates of the fovea and the centre of the optic disc provided by the programme. Subsequently, the pixel coordinates from the markings in the inverted photographs were re-inverted to the original orientation so that the markings of each fovea and optic disc consisted of comparable data from four markings of the same photograph made by each of the four graders. For each photograph, the (x,y) locations of the fovea and the centre of the optic disc at the 16 gradings were averaged, and the distance of each individual marking from this average was noted and transferred to mm at the retinal plane using the algorithm while inserting $n = 6$ mm and $r = 11$ mm. This corresponded to the parameters in Gullstrand's original standard eye (Gullstrand, 1909), which has been confirmed to be representative for larger populations (Rozema et al., 2011).

2.9 | Validation of formalism

The testing of the theoretical and practical limitations of the algorithm was performed using software developed by the first author in C++ (Code Blocks version 20.03, open source).

2.10 | Calculation of space coordinates

The theoretical assumptions of the algorithm were tested by calculations of the space coordinates of the same points marked on fundus photographs with different

centring. Series of fundus photographs were selected from the first 10 patients in the database registered to be born on January 1st and from whom at least five photographs were available. The images were selected from the right eye except for one person in whom only left eye images were available. Eight of the patients had been followed in the department's screening clinic for diabetic retinopathy and the remaining two patients for other retinal diseases.

This resulted in the selection of series with respectively 5, 5, 6, 6, 8, 9, 10, 13, 14 and 29 (in total 105) photographs recorded over an average period of 7.8 years (range 2.6–13.9 years) between 2002 and 2020. The photographs represented all seven digital formats that had been used in the clinic. In 57 of the photographs, the centring had been aimed at the fovea, and in 48 photographs, the centring had been elsewhere, often at or around the optic disc. None of the patients had experienced a change in spherical equivalent refraction of more than 2.75 dioptres during the period or had an astigmatism larger than 1.25 dioptres at any of the examinations.

The Fundus Grading Programme was used by the first author to mark the coordinates of the fovea, the optic disc, and six vascular branching points visible in all photographs of the series, but distributed among different quadrants and at different eccentricities in the fundus. For each marked branching point, the x, y, and z coordinates were calculated using the algorithm with the insertion of $d=6$ mm and $r=11$ mm. The code is available at: https://github.com/Toke-Bek/3D-coordinates-retina.

For each of the marked branching points and the optic disc in the different photographs from each individual, the distance from the mean in the frontal (x,y) plane and in space (x,y,z) was calculated. Subsequently, the mean and the standard deviation of these linear and spatial distances were calculated to describe the reproducibility of the localization of the marked points in the fundus photographs.

2.11 | Ray tracing

The predictions of retinal locations in the used schematic eye were compared to that of an assumed true eye at eccentricities with one-degree intervals from 0 to 30 degrees eccentricity for axial lengths corresponding to ametropia of −6, −3, −1, 0, 1, 3 and 6 dioptres using the open source MATLAB code (https://github.com/gkaguirrelab/gkaModelEye) as described and implemented in the model by Aguirre (2019).

2.12 | Statistical analysis

All statistical analyses were performed using STATA® (version 15.1, College Station, Texas, USA). The data were log-transformed to become normally distributed (Q–Q plots) for the statistical analyses where appropriate.

In the photographs selected to have a clearly discernible fovea and optic disc, the contribution to the variation in the marking of x and y coordinates of the fovea and the centre of the optic disc among image orientations and graders was tested by two-way ANOVA. For each of the 10 photographs, the standard deviation for the repeated markings of the four graders (16 observations) was calculated to represent the reproducibility for each coordinate.

In the series of photographs from patients with retinal disease, the differences from the means of points located on photographs centred around the fovea and photographs centred elsewhere were tested by unpaired t-test.

3 | RESULTS

Table 1 shows that in the fovea-centred images selected to have a clearly discernible fovea and optic disc, the variability in the marking of the fovea by trained graders was higher than that of the optic disc. There was a significant difference between the graders' determination of the foveal y-coordinate (0.0002) and the x-coordinate of the disc centre (0.03), but no significant difference between the markings in the different orientations of the photographs or any of the other comparisons ($p>0.12$ for all comparisons).

Table 2 shows the deviation from the mean of the marked location of branching points and the distance from the fovea to the optic disc centre in the 10 patients with retinal disease. In the overall data set, there was no significant difference in the distances from the mean to the points centred on the fovea ($n=301$) and the points centred elsewhere ($n=256$), neither for distances in the x,y plane ($p=0.74$) nor for distances in the x,y,z space ($p=0.06$).

Figures 4 and 5 show how the variation in the marking of the fovea and the disc centre of the optic disc is translated to variations in the distance between these two points and in the predicted location of the marked branching points in the x,y plane. Figure 4a: The six photographs from Individual 1 who had diabetes with no retinopathy, and Figure 4b: The predicted locations of the optic disc and six branching points from the six photographs in the x,y plane. Figure 5a: Six of the 10 photographs from Individual 7 who had diabetic macular oedema, and Figure 5b: The predicted locations of the optic disc and six branching points from all 10 photographs in the x,y plane. The algorithm displaced the marked location of the fovea to the centre of the coordinate system. Therefore, the variation in the distance between the fovea and the optic disc was a function of the variability in the marking of both the fovea and the optic

TABLE 1 The mean ± SD in the deviations from the mean of the 16 repeated determinations of the x- and y-coordinates to the fovea and the centre of the optic disc.

	Mean ± SD (mm)
Foveal x	0.076 ± 0.095
Foveal y	0.095 ± 0.079
Disc centre x	0.030 ± 0.021
Disc centre y	0.022 ± 0.016
Distance fovea to optic disc	0.081 ± 0.067

TABLE 2 The deviation from the mean of distances in the *x*,*y*-plane and in the *x*,*y*,*z*-space for the location of marked branching points and the distance between the fovea and the optic disc on fundus photographs in different formats and with different centring.

		All branching points		Distance from fovea to optic disc	
Individual	**Image formats (*n*)**	**Deviation from the mean in the *x*,*y* plane mean ± SD (mm)**	**Deviation from the mean in the *x*,*y*,*z* space mean ± SD (mm)**	**Deviation from the mean in the *x*,*y* plane mean ± SD (mm)**	**Deviation from the mean in the *x*,*y*,*z* space mean ± SD (mm)**
1	F4 (2) F7 (4)	0.056 ± 0.027	0.057 ± 0.028	0.044 ± 0.045	0.049 ± 0.047
2	F4 (2) F1 (2) F7 (1)	0.097 ± 0.060	0.101 ± 0.061	0.096 ± 0.048	0.104 ± 0.053
3	F3 (2) F4 (3)	0.180 ± 0.099	0.190 ± 0.105	0.195 ± 0.121	0.212 ± 0.133
4	F3 (6) F5 (2)	0.135 ± 0.094	0.139 ± 0.097	0.091 ± 0.082	0.097 ± 0.090
5	F4 (4) F6 (3) F7 (6)	0.217 ± 0.122	0.228 ± 0.128	0.146 ± 0.145	0.160 ± 0.156
6	F5 (2) F7 (4)	0.180 ± 0.073	0.195 ± 0.081	0.110 ± 0.090	0.123 ± 0.096
7	F4 (4) F5 (6)	0.226 ± 0.115	0.243 ± 0.125	0.159 ± 0.092	0.174 ± 0.100
8	F4 (7) F5 (2)	0.141 ± 0.078	0.153 ± 0.084	0.124 ± 0.088	0.134 ± 0.096
9	F2 (2) F3 (2) F4 (4) F5 (2) F7 (4)	0.150 ± 0.098	0.161 ± 0.105	0.140 ± 0.114	0.152 ± 0.124
10	F4 (11) F5 (5) F6 (2) F7 (11)	0.203 ± 0.111	0.213 ± 0.117	0.100 ± 0.093	0.108 ± 0.099
Mean		0.158 ± 0.088	0.168 ± 0.093	0.121 ± 0.092	0.131 ± 0.099

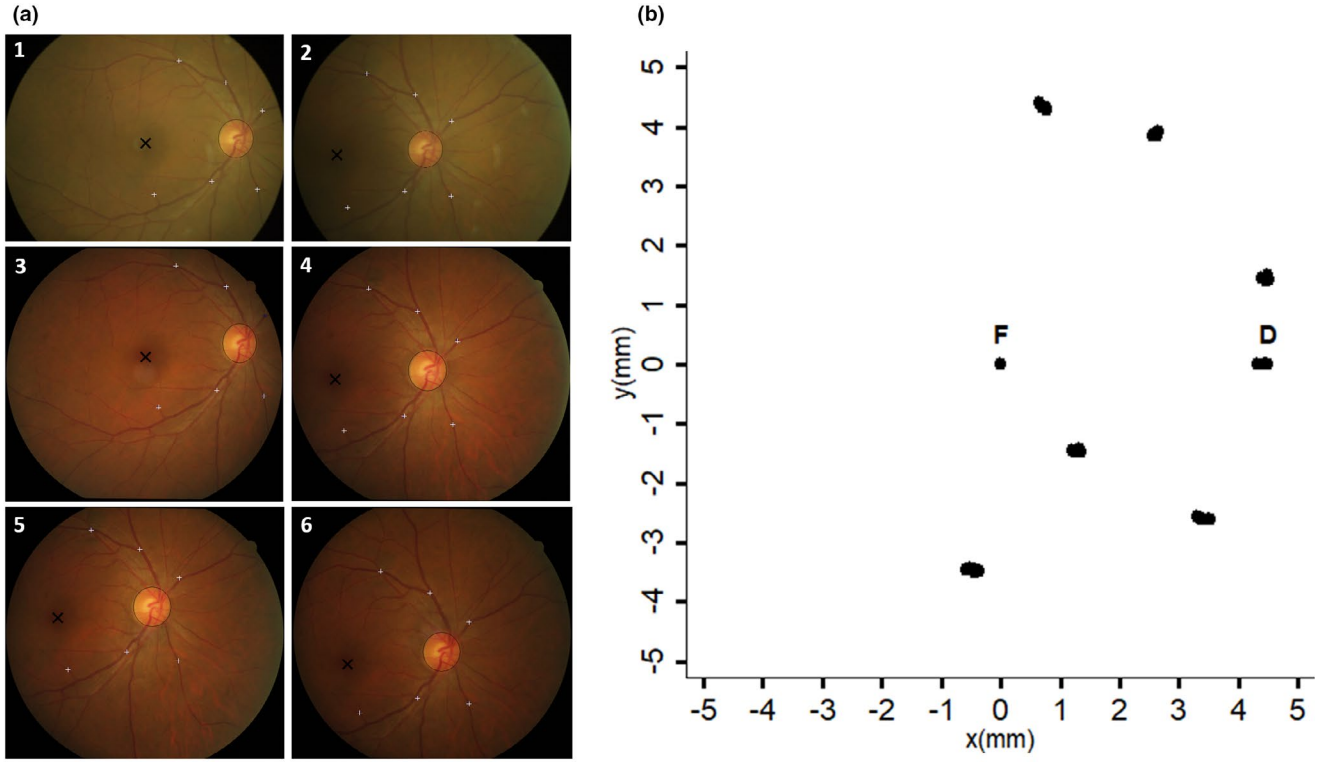

FIGURE 4 (a) The six photographs in the series from Patient 1 who had no retinopathy. The marking of the fovea is shown with a black cross, the optic disc by the best fitting ellipse and the vascular branches with small white crosses. (b) The calculated *x*,*y* coordinates of the optic disc centre and the six branching points from the six photographs from individual 1 in Table 2 and this figure, where the variation from the mean of predicted locations on the retina was low.

disc in the photographs. The variation in the marking of the branching points on the photographs also contributed to the variation in the predicted location of these points in the retina.

The ray tracing experiments showed that the variability in the localization of a point on the retina was within 50 μm within four degrees eccentricity in an emmetropic eye, within seven degrees in an eye with −1D myopia and within 15 degrees in an eye with −3D myopia.

4 | DISCUSSION

The algorithm derived to transform locations in a two-dimensional fundus photograph to spatial locations in the retina rested on several assumptions. First, the testing of the employed fundus cameras in an eye model confirmed that equiangular distances were imaged equidistantly on the photographic film (Littmann, 1982). This was the background for the assumption of a simple linear relation between a distance in the photograph and a nodal angle, which cannot be assumed per se (Pors et al., 2024). The focussing of the retina in ametropic eyes will introduce a change in magnification (Garway-Heath et al., 1998), but previously measured effects of less than one per cent per dioptre ametropia can be considered not to affect the results of the present study significantly (Bek & Lund-Andersen, 1990; Rudnicka et al., 1998) and are described in Equation (1). Second, the algorithm required assumptions of distances in the third dimension along the *z*-axis that are not available with the information contained in a fundus photograph. This dimension was represented by the curvature radius (*r*) of the eye set to 11 mm and the distance from the nodal point to the centre of the eye (*d*) set to 6 mm in accordance with Gullstrand's normal eye (Gullstrand, 1909) and confirmed post mortem in human eyes (Mohamed et al., 2021). However, in clinical practice, *r* and *d* will be individually varying (Rozema et al., 2011), and the curvature radius of the eye varies among the centre and the periphery of the fundus, among different quadrants within the same individuals (Minami et al., 2020), and in retinal disease (Luo et al., 2023). Additionally, the location of the nodal point may not be the same for rays entering the eye to extrafoveal points (Harris, 2010). This underlines that the calculation of absolute distances on the retina requires the inclusion of more anatomical data than included in the present study. Due to these limitations, the presented algorithm cannot predict the absolute location of positions on the retina, but defines the limitations for studying changes in the location of morphological lesions over time within the same eye as validated in a series of fundus photographs from the same individual. Under the assumption of the dimensions of Gullstrand's standard eye, the variation in the distance from the mean of calculated coordinates in the *x*,*y*,*z*-space was only slightly larger than the variation in the calculated coordinates in the *x*,*y*-plane. This suggests that the variation of the assumed *r* and *d* values from the true values in the *z*-direction had only a minimal effect on the intra-individual variability in the marking of points in photographs obtained with different centring. However, deviations in the assumed from the true values

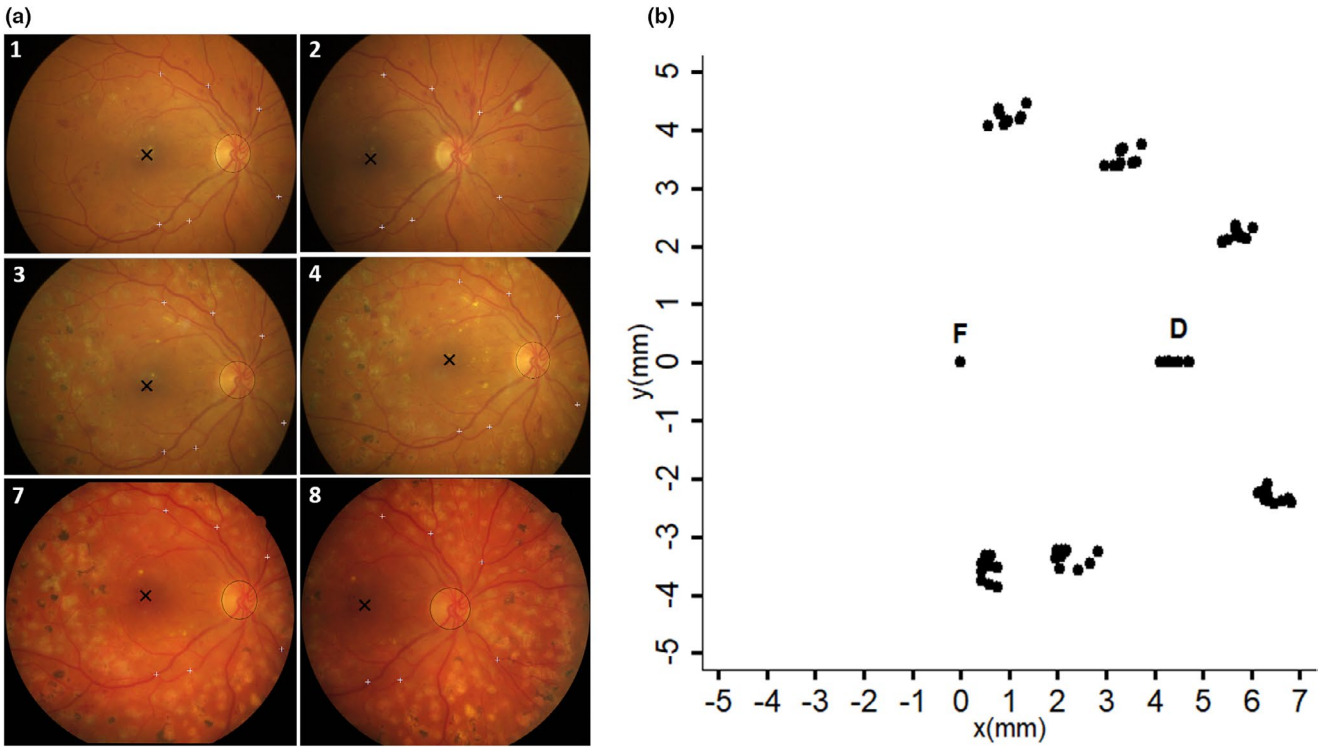

FIGURE 5 (a) Photographs 1–4 and 7–8 in the series from Patient 7 who had diabetic maculopathy and was treated with retinal photocoagulation. The marking of the fovea is shown with a black cross, the optic disc by the best fitting ellipse and the vascular branches with small white crosses. (b) The calculated *x*,*y* coordinates from the optic disc centre and the six branching points from all 10 photographs from Individual 7 in Table 2, where the variation from the mean of predicted locations on the retina was high.

for r and d, and thereby the size and shape of the eye, will inherently affect the prediction of the true values of *x*,*y*,*z* coordinates on the retina. It should therefore be the subject of a future study to investigate the significance of including individual values for r and d obtained from biometry and scans of the shape of the posterior segment of the eye in the model. The ray tracing experiments confirmed that the observed variability of 50 µm in the prediction of locations 15 degrees from the fovea corresponding to approximately 5 mm from the fovea in Gullstrand's eye was realistic.

A precondition for reproducing the calculation of space coordinates is to define an initial system as an outset for these coordinates. The use of the fovea and the optic disc precluded the use of the algorithm on photographs where one of these points was not represented and was limited by the accuracy in the identification of these references. In the set of photographs with clearly discernible fovea and optic disc, the marking of the centre of the optic disc could be estimated with a low variability because the centre of the ellipse fitted to the disc margin depended on the delimitation of the disc from all sides and therefore was less sensitive to variations in the graders' individual definitions of the transition of the disc areas to the surrounding retina. The higher variability in the manual marking of the fovea, especially in the vertical plane, may be due to a less distinct appearance of this structure in the fundus photograph, even in individuals where this structure is seemingly easy to identify. The fact that the definition of *x*,*y* coordinates to the fovea and the optic disc centre was independent of the rotation of the test images supports that the variability in the identification of these structures should be similar among right and left eyes. However, the significant difference in the variation among the graders indicates that there are limitations in the manual marking of the reference points. This inter-individual variability may also explain the larger variation in the distance between the fovea and the optic disc observed among different graders in the same images than in the image series with no retinopathy marked by the same grader where the determination of this distance was more consistent.

The fovea was assumed to represent the centre for concentrical changes in the curvature radius of the eye. This assumption disregards the separation of the visual axis passing through the fovea with an angle kappa from the geometric axis of the eye, a deviation that is especially pronounced in patients with eccentric fixation (Berrio et al., 2010). The variation in the definition of foveal coordinates translates to a variation in the decentring which, together with the variation in the definition of the optic disc, translates to a variation in the definition of the reference meridian for describing the *x*,*y*,*z* coordinates. In the series of photographs from patients with retinal disease, the variability in the spatial prediction of the optic disc and the branching points was generally larger than in the photographs from persons without retinal disease, and the three patients in whom the variation was largest also had macular oedema. This points to significant limitations for the use of the method in patients with macular disease where the fovea is difficult to discern. Therefore, in a future study, the algorithm should be tested on images where locations in the retina, especially the fovea but also the optic disc, are identified with more objective and reproducible methods such as with automated software.

The spatial resolution of retinal objects imaged through the optics of a standard Gullstrand eye with a dilated pupil to a photographic film should theoretically be approximately 1.5 µm at wavelengths around 500 nm (Rubin, 1993). With the nodal length of the eye set to 18 mm, this corresponds to an angular subtense of approximately 0.02 degrees, requiring a resolution of 50 pixels per degree in the fundus photograph. This is standard in modern digital fundus cameras, and all the employed image formats in the present study had this minimum resolution. However, this is far from what can be obtained in practice because of limitations in the optics of the eye and the low contrast between especially red lesions in the retina and the background. The radial compression of the image predicted in the present study implies that the resolution would be up to 1.6 times lower in the periphery than in the centre of a 60 degrees fundus photograph, which is comparable to previously published estimates (Croft et al., 2014). This implies that a lesion with a size near the detection limit in the central area of the retina may be invisible if it is located in the retinal periphery. This should be considered in the evaluation of fundus photographs of retinal disease.

The findings of the present study have several implications. The compression of radial distances in the periphery of fundus photographs is tied to the location of the nodal point anterior to the centre of the eye and therefore also applies for other imaging modalities such as ophthalmoscopy. This implies that the clinical experience of how the peripheral retina appears morphologically does not reflect the true appearance of these areas. The true size of lesions in the retinal periphery is larger than they appear and their shape is radially compressed. This may aggravate the impression of an ovoid shape of the optic disc with the short axis in the horizontal (radial) direction which is supported by studies showing that the optic disc is histologically approximately 6% taller than it is wide (Quigley et al., 1990), whereas the percentage is higher when determined by planimetry from fundus photographs (Jonas et al., 1999; Neubauer et al., 2006). We have confirmed this in preliminary experiments where the optic disc documented by fundus photography in vivo was photographed immediately after removal of the optics of an eye enucleated because of a choroidal melanoma. The finding may also have implications for the calculation of the diameter of the larger vascular arcades. Thus, the cross sections of the temporal vascular arcades nearly coincide with (radial) meridians from the fovea, which will lead to an underestimation of the diameter of these vessels, whereas the nasal vascular arcades will tend to be oriented more along these radians with a less significant influence of radial compression on the cross-sectional diameter. This may affect measurements of the distribution of blood flow to different areas of the retina (Jeppesen & Bek, 2019; Jørgensen & Bek, 2017). The radial compression may also have implications for the evaluation of angles of vascular bifurcatures that are considered as risk factors for systemic vascular disease (Klein et al., 2018; Shen Lim et al., 2011). These angles may appear falsely too acute at orientations along radians and too obtuse at orientations perpendicular to the radians. Therefore, findings of the study document the limitations in assessing the severity and following the progression of retinal disease based on a detailed grading of morphological lesions from fundus photographs.

In conclusion, the present study describes and assesses the reproducibility of an algorithm to align retinal locations on serial fundus photographs from assumed axial distances in the eye together with the location of the fovea and the optic disc. The study defines limits for studying changes in shapes, locations, distances and areas of retinal lesions in fundus photographs over time.

ACKNOWLEDGEMENTS

Consultant Line Petersen and nurse graders Helle Hedegaard, Tina Bjerre and Anita Düring are thanked for performing the masked grading of the fovea and the optic disc.

CONFLICT OF INTEREST STATEMENT

None. The study was performed as part of the authors' academic affiliations.

ORCID

Toke Bek https://orcid.org/0000-0002-0409-2534
Giovanni Ometto https://orcid.org/0000-0002-0900-4847

REFERENCES

Aboshiha, J., Dubis, A.M., van der Spuy, J., Nishiguchi, K.M., Cheeseman, E.W., Ayuso, C. et al. (2015) Assessment of accuracy and precision of quantification of ultra-widefield images. *Ophthalmology*, 122(4), 864–866.

Aguirre, G.K. (2019) A model of the entrance pupil of the human eye. *Scientific Reports*, 9, 9360.

Aldington, S.J., Kohner, E.M., Meuer, S., Klein, R. & Sjølie, A.K. (1995) Methodology for retinal photography and assessment of diabetic retinopathy: the EURODIAB iDDM complications study. *Diabetologia*, 38(4), 437–444.

Bek, T. & Lund-Andersen, H. (1990) Accurate superimposition of perimetry data on fundus photographs. *Acta Ophthalmologica*, 68(1), 11–18.

Bennett, A.G., Rudnicka, A.R. & Edgar, D.F. (1994) Improvement on Littman's method for determining the size of retinal features by fundus photography. *Graefe's Archive for Clinical and Experimental Ophthalmology*, 232, 361–367.

Berrio, E., Tabernero, J. & Artal, P. (2010) Optical aberrations and alignment of the eye with age. *Journal of Vision*, 10(14), 34.

Croft, D.E., van Hemert, J., Wykoff, C.C., Wykoff, C.C., Clifton, D., Verhoek, M. et al. (2014) Precise montaging and metric quantification of retinal surface area from ultrawidefield fundus photography and fluorescein angiography. *Ophthalmic Surgery, Lasers & Imaging Retina*, 45, 312–317.

Garway-Heath, D.F., Ruben, S.T., Viswanathan, A. & Hitchings, R.A. (1998) Vertical cup/disc ratio in relation to optic disc size: its value in the assessment of the glaucoma suspect. *The British Journal of Ophthalmology*, 82(10), 1118–1124.

Gullstrand, A. (1909) *Appendix II and IV. von Helmholtz' Handbuch der Physiologischen Optik*, Vol. 1, 3rd edition. Hamburg, Germany: Voss, pp. 301–358, 382–415.

Harris, W.F. (2010) Nodes and nodal points and lines in the eyes and other optical systems. *Ophthalmic and Physiological Optics*, 30(1), 24–42.

Jeppesen, S.K. & Bek, T. (2019) The retinal oxygen saturation measured by dual wavelength oximetry in larger retinal vessels is influenced by the linear velocity of the blood. *Current Eye Research*, 44(1), 46–52.

Jonas, J.B., Budde, W.M. & Panda-Jones, S. (1999) Ophthalmoscopic evaluation fo the optic nerve head. *Survey of Ophthalmology*, 43(4), 293–320.

Jørgensen, C.M. & Bek, T. (2017) Lack of differences in the regional variation of oxygen saturation in larger retinal vessels in diabetic maculopathy and proliferative diabetic retinopathy. *The British Journal of Ophthalmology*, 101(6), 752–757.

Klein, R., Lee, K.E., Danforth, L., Tsai, M.Y., Gangnon, R.E., Meuer, S.E. et al. (2018) The relationship of retinal vessel geometric characteristics to the incidence and progression of diabetic retinopathy. *Ophthalmology*, 125(11), 1784–1792.

Luo, N., Wang, Y., Alimu, S., Zhao, L., Huang, Y., Guo, Z. et al. (2023) Assessment of ocular deformation in pathologic myopia using 3-dimensional magnetic resonance imaging. *JAMA Ophthalmology*, 141(8), 768–774.

Minami, S., Ito, Y., Ueno, S., Kataoka, K., Takeuchi, J., Ito, H. et al. (2020) Analysis of macular curvature in normal eyes using swept-source optical coherence tomography. *Japanese Journal of Ophthalmology*, 64(2), 180–186.

Mohamed, A., Nandyala, S., Ho, A., Manns, F., Parel, J.-M.A. & Augusteyn, R.A. (2021) Relationship of the cornea and globe dimensions to the changes in adult human crystalline lens diameter, thickness and power with age. *Experimental Eye Research*, 209, 108653. Available from: https://doi.org/10.1016/j.exer.2021.108653

Neubauer, A.S., Krieglsterin, T.R., Chryssafis, C., Thiel, M. & Kampik, A. (2006) Comparison of optical coherence tomography and fundus photography for measuring the optic disc size. *Ophthalmic & Physiological Optics*, 26(1), 13–18.

Pors, L.J., Corné, H., van Vught, L., Hoes, N.P., Luyten, G.P., van Rijn, G.A. et al. (2024) Correction method for optical scaling of fundoscopic images: development, validation, and first implementation. *Investigative Ophthalmology & Visual Science*, 65(1), 43.

Quigley, H.A., Brown, A.E., Morrison, J.D. & Drance, S.M. (1990) The size and shape of the optic disc in the normal human eye. *Archives of Ophthalmology*, 108(1), 51–57.

Rozema, J.J., Atchison, D.A. & Tassignon, M.-J. (2011) Statistical eye model for normal eyes. *Investigative Ophthalmology & Visual Science*, 52(7), 4525–4533.

Rubin, M.L. (1993) *Optics for clinicians*. Gainesville, FL: Triad Publishing Company, p. 340.

Rudnicka, A.R., Burk, R.O.W., Edgar, D.F. & Fitzke, F.W. (1998) Magnification characteristics of fundus imaging systems. *Ophthalmology*, 105, 2186–2192.

Shen Lim, L., Cheung, C.Y.-I., Lin, X., Mitchell, P., Wong, T.Y. & Mei-Saw, S. (2011) Influence of refractive error and axial length on retinal vessel geometric characteristics. *Investigative Ophthalmology & Visual Science*, 52(2), 669–678.

Spaide, R.F. (2011) Peripheral areas of nonperfusion in treated central retinal vein occlusion as imaged by wide-field fluorescein angiography. *Retina*, 31, 829–837.

Zhang, J., Wen, B., Kalaw, F.G.P., Kavichine, M., Bartsch, D.-U.G., Freeman, W.R. et al. (2023) Accurate registration between ultra-wide-field and narrow angle retina images with 3D eyeball shape optimization. *Proceedings of International Conference on Image Processing*, 2023, 2750–2754. Available from: https://doi.org/10.1109/icip49359.2023.10223163

How to cite this article: Bek, T. & Ometto, G. (2026) Reproducibility in the identification of retinal positions on serial fundus photographs: Theory and limitations. *Acta Ophthalmologica*, 104, 201–211. Available from: https://doi.org/10.1111/aos.17566

APPENDIX A

From Figure 2, it appears that the tangent to the nodal angle ν_P can be expressed as:

$$\tan(\nu_P) = \frac{a}{b+d} \tag{A1}$$

Additionally, from Figure 2, the distances a and b can be expressed as:

$$a = r * \sin(\omega_P) \tag{A2}$$

$$b = r * \cos(\omega_P) \tag{A3}$$

The substitution of (A1) with the expressions for a in (A2) and for b in (A3) yields:

$$\tan(\nu_P) = \frac{r * \sin(\omega_P)}{r * \cos(\omega_P) + d}$$

We can rearrange the equation to express the denominator:

$$r * \cos(\omega_P) + d = \frac{r * \sin(\omega_P)}{\tan(\nu_P)}$$

Then, after squaring both sides:

$$r^2 * \cos^2(\omega_P) + d^2 + 2 * d * r * \cos(\omega_P) = \frac{r^2 * \sin^2(\omega_P)}{\tan^2(\nu_P)}$$

we can rewrite the equation using the identity: $\sin^2(\omega_P) = 1 - \cos^2(\omega_P)$ to result in:

$$r^2 * \cos^2(\omega_P) + d^2 + 2 * d * r * \cos(\omega_P) = \frac{r^2 * (1 - \cos^2(\omega_P))}{\tan^2(\nu_P)}$$

We can now separate the terms involving $\cos(\omega_P)$

$$r^2 * \cos^2(\omega_P) + d^2 + 2 * d * r * \cos(\omega_P) = \frac{r^2}{\tan^2(\nu_P)} - \frac{r^2 * \cos^2(\omega_P)}{\tan^2(\nu_P)}$$

and combine the elements to form a quadratic equation in terms of $\cos^2(\omega_P)$

$$\cos^2(\omega_P) * \left(r^2 + \frac{r^2}{\tan^2(\nu_P)}\right) + \cos(\omega_P) * (2 * d * r) + \left(d^2 - \frac{r^2}{\tan^2(\nu_P)}\right) = 0$$

We can now find the solution for $\cos(\omega_P)$ using the quadratic formula:

$$\cos(\omega_P) = \left(\frac{-2*d*r \pm \sqrt{4*d^2*r^2 - 4*\left(r^2 + \frac{r^2}{\tan^2(v_P)}\right)*\left(d^2 - \frac{r^2}{\tan^2(v_P)}\right)}}{2*\left(r^2 + \frac{r^2}{\tan^2(v_P)}\right)} \right)$$

Finally, we can simplify and solve for ω_P using the arccosine function:

$$\omega_P = a\cos\left(\frac{-d*\tan(v_P) \pm \sqrt{r^2*\left(1 + \frac{1}{\tan^2(v_P)}\right) - d^2}}{r*\left(\tan(v_P) + \frac{1}{\tan(v_P)}\right)} \right)$$

In the normal eye, it can be assumed that d is always smaller than r. Therefore, the formula under the square root is always positive, leading to a real solution. If point P is in the rear hemisphere of the eye, it follows that $(0 < \omega_P < \pi/2)$. Thereby, the argument of $a\cos$ in the equation must be positive. Since the denominator of this argument is always positive, and the first term of the numerator is negative, we should only consider the positive sign in the solution of the quadratic formula:

$$\omega_P = a\cos\left(\frac{-d*\tan(v_P) + \sqrt{r^2*\left(1 + \frac{1}{\tan^2(v_P)}\right) - d^2}}{r*\left(\tan(v_P) + \frac{1}{\tan(v_P)}\right)} \right) \quad \text{(A4)}$$